Spatial Temperature Profiles in an Aluminum Reduction Cell under Different Anode Current Distributions

Cheuk-Yi Cheung, Chris Menictas, Jie Bao, Maria Skyllas-Kazacos, and Barry J. Welch
School of Chemical Engineering, The University of New South Wales (UNSW), Sydney, NSW 2052, Australia

DOI 10.1002/aic.13942
Published online November 15, 2012 in Wiley Online Library (wileyonlinelibrary.com).

The development of a thermal model to estimate energy distribution in an aluminum reduction cell and its impact on local conditions based on anode current signals are presented. In the Hall–Héroult process, routine practices carried out during operation give rise to spatial energy imbalances and consequently temperature variation in the cell. This phenomenon has been ignored in thermal models developed to date as they are only concerned with overall process dynamics. Implementing anode current signals as model inputs along with the discretization method allows the change of spatial conditions caused by current distribution to be calculated. Simulation studies have been performed to investigate the cell thermal balance affected by anode shorting. The article shows the potential of using anode current signals as model inputs to compute spatial thermal conditions based on the proposed model structure that are not considered in traditional modeling approaches. © 2012 American Institute of Chemical Engineers *AIChE J,* 59: 1544–1556, 2013
Keywords: aluminum smelting, dynamic model, spatial energy distribution, anode current distribution

Introduction

One important aspect to be controlled in the Hall–Héroult process is the thermal balance in the reduction cells. A well-maintained thermal balance provides the foundation for better operation and process efficiency.[1,2] However, the nature of the process introduces disturbances to different parts of the cell during the operation. Routine practices such as alumina feeding and anode replacement disturb the local thermal balance on a regular basis. Examples of spatial variations in bath temperature are illustrated in the literatures.[3,4] They show temperature distribution can be uneven under normal operation. Thermal imbalance invariably gets worse when an anode is replaced. Its impact can prolong beyond 24 h after an anode replacement. These studies suggest that a single measurement does not give a representative reading of bath temperature across the cell. It merely reflects the local thermal condition at the time where it is measured. Nevertheless, the general practice in industry is to observe the thermal condition of a reduction cell by a single bath temperature measurement conducted daily. Spatial variation is generally ignored and assumed to be insignificant. This assumption might not be met in practice particularly with recent advances that places an emphasis on increasing amperage to maximize productivity.[5–7] Amperage, referred to as the line current, is the total current fed into a reduction cell that determines the theoretical amount of aluminum metal produced per cell. The implementation of higher amperage on the process leads to the development of larger reduction cells.[8] Spatial variations in larger cells are more significant and pose greater influences on process behavior.[6,7–9] Because it is difficult to observe their impacts on the cell thermal balance using direct measurements, development of thermal models is important for prediction and estimation of the cell conditions to achieve better control, especially in large reduction cells.

Various models have been developed to estimate thermal balances of reduction cells.[10–16] These models rely on conventional measurements of cell voltage V_{cell}, and line current as primary model inputs to calculate the total energy input across the entire cell. They predict overall dynamic responses and, therefore, impacts of local thermal disturbances on the cell condition are ignored. Most of the models include heat transfer induced by bath flow by using a higher bath thermal conductivity. Taylor et al.,[17] on the other hand, discretizes the cell into tank-pipe systems to compute local thermal balance caused by the bath flow. The model structure allows the calculation of local bath temperature of different areas; however, it does not attempt to calculate the horizontal ledge profile. The ledge is a layer of frozen primary crystallizing phase of the electrolyte formed along on the surface of the sidewall in contact with the electrolyte. Cell thermal and material balances are sensitive to the change of ledge profile. In this article, the proposed model allows the computation of the horizontal ledge profile along the sidewall. Although most of the models found in the literature incorporate cell voltage and line current measurements, fewer models which use anode current measurements have been developed.[3,18] They studied the change of spatial conditions, yet their emphases are not on dynamic changes of thermal balance.

This article presents a dynamic model to study thermal variations in a reduction cell under the influence of anode current distribution. As local anodic activities and bath

Correspondence concerning this article should be addressed to J. Bao at j.bao@unsw.edu.au.

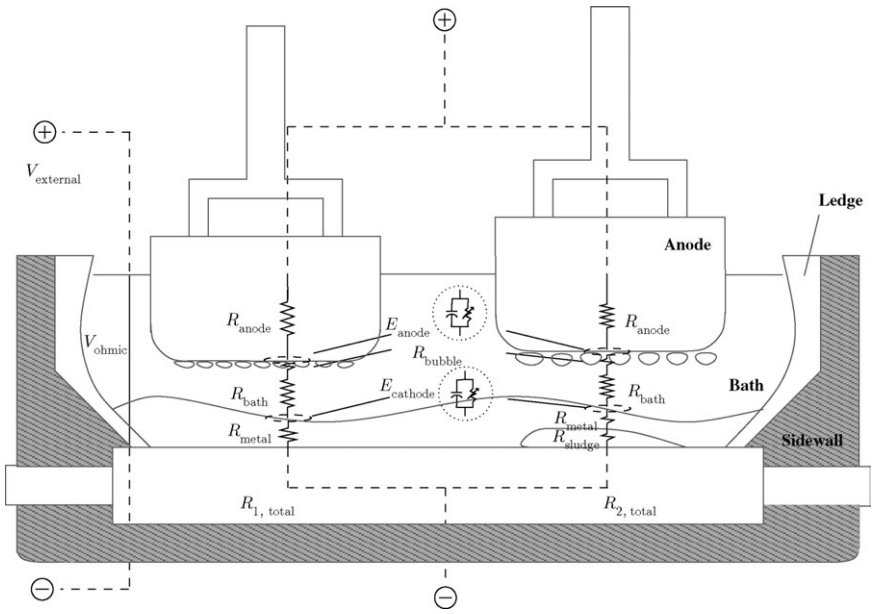

Figure 1. Schematic diagram of a reduction cell and a resistance network.

conditions in the vicinity of the anodes determine the current distribution, implementation of anode current signals as model inputs allows estimation of local cell dynamics. The model is discretized into a two-dimensional (2-D) array of subsystems based on anode locations to capture local energy inputs induced by anode current flows. It allows estimation of the spatial temperature variation in a reduction cell when measurements are limited. Detection of potential problems that are usually not visible with conventional measurements can be achieved and hence local thermal imbalance can also be identified. The development of the model proposed in this article extends the simpler models derived in the authors' earlier works.[19–21]

The article is structured as follows: the nature of the Hall–Héroult process and the use of anode current measurements for cell monitoring are described in the Background section. The model discretization method and the implementation of anode current signals as model inputs are illustrated in the Modeling Approach section. Model features are then discussed. Different types of heat balances with different heat exchange interfaces present in the model as a function of the subsystem locations are demonstrated. Model validation and simulation studies of anode shorting are presented, followed by Conclusions and Future Development.

Background

Process description

Coupled Mass and Thermal Balance. The Hall–Héroult process solely relies on electricity to maintain heat balance and drive the electrochemical reaction for metal production.[22–24] It takes place in a cell filled with electrolyte referred to as "the bath." A portion of the bath is allowed to freeze along the cell sidewall (see Figure 1). This freeze acts as a protective barrier for the sidewall. The existence of the freeze, referred to as the ledge, creates interactions between the mass and thermal balance. Its thickness and profile along the cell are significant factors to keep this coupled effect stable as they determine the rate of heat loss from the cell and bath composition. The interfacial temperature is usually at the liquidus temperature T_{Liq}, as a consequence of selected operating conditions. The thermal driving force that governs the ledge thickness and profile is called the superheat ΔT_{SH}, and is defined as follows

$$\Delta T_{SH} = T_b - T_{Liq}. \tag{1}$$

The major factor that leads to changes in bath temperature T_b, is the heat imbalance in the cell. Liquidus temperature can be altered by the change of bath composition. Changes in either of the temperatures can cause variations in the superheat. This variation leads to ledge freezing or melting and, thus, a change in ledge thickness. Such change affects the horizontal thermal resistance through the sidewall as well as the bath composition ($Al_2O_3 + AlF_3 + CaF_2$ + cryolite) because the composition of the freeze is closer to that of pure cryolite.[1] The rate of heat dissipation and the solidification point change, and, therefore, the bath and liquidus temperature vary accordingly. This cycle ends when both temperatures and other parameters associated to the cell reach another steady state before the balance is again disturbed. In the case where local variations arise, the superheat at different parts of the cell would be different, consequently causing different degrees of ledge melting and freezing. Therefore, the ledge profile along the cell is always nonuniform.

Path Resistance. In the reduction process, liquid aluminum deposits and forms a pool of conductive liquid on the cathode assembly and becomes part of the cathode. A number of consumable carbon anodes are suspended and partly immersed in the bath. These are supported by anode beams, leaving a gap between the bottom of the anodes and the liquid cathode surface. The gap height is named the anode cathode distance (ACD).[1,25] During operation, electrical current enters the cell through the anode beams and is distributed among all operating anodes. It flows into separate pathways formed by the anodes and then reassembles at the cathode. As the anode resistance is less than the bath resistance, most current leaves the anodes from the bottom instead of

the side. As a result, the current flow creates an electrical network consisting of parallel circuits with a structure determined by the anode arrangement. Path resistances in those parallel circuits are responsible for the ohmic heat generation within the cell. Those resistances are made up of different components. The major physical components are layered as follows: anode, bubbles generated by anodic reactions, the bath, and the metal. Their resistances are often of different magnitudes due to distinct local electrochemical dynamics. The interfacial voltage drops caused by anodic reactions and cathodic reactions are denoted by E_{anode} and E_{cathode}, respectively in Figure 1. Each voltage drop includes the electrode potential for the respective reaction and overpotentials associated with the reaction rate. As electrochemical reactions and their rates are electrode potential-dependent, the representation of the interfacial voltage drop is a capacitor and variable resistor connected in parallel. However, it can be treated as a resistance for the computation of the energy balance to determine heat generation as a consequence of the overpotentials dissipating energy as heat. The heat dissipation contributes to extra heat generation on top of the heat generated through the physical components. There are also a number of factors that may affect the path resistance. Anode age, metal pad instability, and short circuiting of an anode with the metal layer are some of the examples. Abnormalities, such as short circuiting, usually arise at a localized level and affect local resistance. Therefore, the overall resistance in each path can be different based on the electrochemical dynamics and local bath conditions. Figure 1 shows a network of electrical resistance components at different anodes. Two examples $R_{1,\text{total}}$ and $R_{2,\text{total}}$ show the total path resistances in different local environments with $R_{2,\text{total}}$, including the resistance of the sludge. Physical properties and the depth of each component layer determine the corresponding electrical resistance as demonstrated in the figure. Sludge is a two-phase slurry consisting of cryolite-rich electrolyte saturated with alumina and undissolved alumina. It can accumulate either in piles at the side of the cell cavity, extending through the metal to the electrolyte, or as a layer on top of the cathode blocks. Consequently, it can give rise to a localized increase of electrical resistance. Thus, path resistance often varies with time as well as location. In the present model, the path resistance considered is restricted from the bath surface to the cathode assembly surface as shown in the solid line in the schematic diagram.

As voltage in each path of the parallel circuit is always the same, the magnitude of current flows in each anode changes accordingly with the overall path resistance. This implies that the change reflects the variation of the dynamic behavior and the surrounding condition at the corresponding anode. Hence, local information of the cell can be extracted from the measurements of the current running through each anode. This split current is usually referred to as the anode current.[9] As the total amperage of all anode currents (line current) is regulated by rectifiers, the magnitudes of anode currents are always interdependent of each other. In cases such as anode shorting or improperly set anodes, some anodes may carry a greater current load, leading to uneven current distribution in the cell. The prolonged presence of this current unevenness can cause thermal imbalance and lead to a deterioration in cell performance.[7,26–28] It is always desirable to avoid any situation that leads to uneven current distribution during operation.

Local Ohmic Heat Generation. When electricity passes through a resistance block, energy is dissipated in the form of heat due to the ohmic effect. The implementation of high amperage in the Hall–Héroult process leads to significant ohmic heat generation in the cell that is responsible for maintaining bath temperature around 960°C without any external heating sources. The overall ohmic heat generation in the liquid region is the product of amperage and voltage drop across the bath and metal. This voltage drop only includes components in the current path that contribute to heat generation but not consumed by chemical reactions. It is illustrated in Figure 1 and is calculated by

$$V_{\text{ohmic}} = V_{\text{cell}} - V_{\text{external}} - E_{\text{production}}, \tag{2}$$

where $E_{\text{production}}$ is the equivalent voltages for electrochemical reactions of metal production, including feed heating and dissolution. The external voltage drop that occurs outside the bath is denoted by V_{external}. As anode current I_{an}, provides the total energy flowing into each anode, ohmic heat generation through each current path q_{ohmic}, can be determined by the anode currents when used as model inputs as follows

$$q_{\text{ohmic}} = V_{\text{ohmic}} \cdot I_{\text{an}}. \tag{3}$$

Although "fanning" of the anode current occurs around the periphery of each anode, the heat generation caused by this effect is relatively small as the bubble layers underneath anodes have higher resistance than the bath. Therefore, this thermal effect is not considered. In this work, it is assumed that anode current travels vertically from the anode to the cathode and generates heat in the physical components where it passes. Those physical components are anodes, the bubble layers as well as the liquids underneath the anodes. Therefore, this term is included to the heat equation of subsystems only if an anode is present, which will be discussed further in the later section. The introduction of this new model inputs allows capturing the change of energy flow into different parts of the cell, leading to a more accurate computation of spatial heat generation when current distribution is uneven.

Anode current measurements

The concept of extracting more cell information from individual anode currents was proposed in the literatures. Supervision of the cell condition by monitoring the current distribution alone was patented in the 1980s.[29] More works have been carried out to measure and use this information.[30–32] The purpose of introducing anode current measurements in cell monitoring compensates for the lack of available data that can be obtained from conventional measurements. The nature of the Hall–Héroult process imposes significant limitation on the measurements that can be carried out in the bath online due to technical infeasibility.[33] Therefore, cell monitoring and control in all smelters highly relies on continuous measurements of cell voltage and line current. They provide a view of global cell conditions and occurrences of some abnormalities. However, they are unable to reveal spatial dynamic variations. As a result, it is difficult to identify the location where local abnormalities occur, especially a local thermal imbalance using cell voltage and line current.

Anode current signals, on the other hand, provide spatial information of the cell. Their magnitudes reflect anodic process dynamics as well as bath conditions in the vicinity of the corresponding anode. The application of this measurement to an operating cell can be used to monitor instant cell

condition and to detect local abnormalities based on their magnitudes.[9,32,34–37] By observing the overall distribution, the degree of metal instability can be evaluated based on the degree of anode current fluctuations. Any unusually high current pickup would indicate when the ACD of an anode becomes comparatively shorter, thus inducing more current to be drawn by that particular anode.[33] This phenomenon can be caused by a spiked anode or an anode positioned too low into the bath leading to, as a worst case scenario, short circuiting with the liquid metal cathode. The trend of anode current variation can also provide an early indication of an onset of anode effect.[37] A sudden decrease in the magnitude of an anode current signal could indicate the beginning of a localized anode effect before it propagates throughout the cell. As the occurrence of an anode effect always causes an abrupt increase on the cell voltage,[38,39] conventional cell monitoring only allows its detection when damage to the cell is already occurring by the excessive energy input. This is the same for other local abnormalities that are less easily identified by conventional continuous measurements, especially local thermal imbalance that is hard to observe.

Although there is a growing interest in anode current measurements, their application is usually limited to cell monitoring. The anode current signals do not just reflect individual dynamics at anodes; however, they also indicate energy inputs to different parts of a cell. That means energy distribution within the cell can be deduced by current distribution. Local bath temperature and, therefore, local superheat can be estimated based on this information. Hence, ledge thickness at different locations of the cell can be predicted to deduce its cross sectional profile. Variations of other cell parameters that are dependent on the change of ledge thickness, for instance, bath height and volume as well as liquidus temperature can also be estimated in a finer manner. Therefore, anode current signals have additional advantages over conventional measurements when implemented in thermal modeling as local thermal conditions and their impacts on the local ledge thickness can be computed.

Modeling Approach

Proposed model discretization

The model is separated into three major regions. These are the liquid, ledge, and sidewall. The liquid region comprises bath and metal layers in the cell cavity as well as components immersed within, including anodes. The ledge region is defined to be the solid bath formed along the sidewall. The sidewall region represents the cell structure with fixed boundary. As ledge thickness can change due to the coupled effect discussed previously, the boundary of the bath and ledge region can move during simulations, and, thus, change the volumes of the regions. In addition, as the sum of bath and metal height defines the path resistance considered in this modeling approach, the control volumes also vary in a vertical direction.

An illustrative diagram of the discretization of a simplified reduction cell as viewed from the top is shown in Figure 2. As current enters the cell through anodes, the location of anodes and the magnitude of anode currents determine the energy distribution across the cell. To capture the spatial variations caused by current distribution, the bath and the ledge regions are further discretized into a 2-D array of subsystems based on anode locations as represented by the dotted lines in the figure. Such a spatial discretization is needed

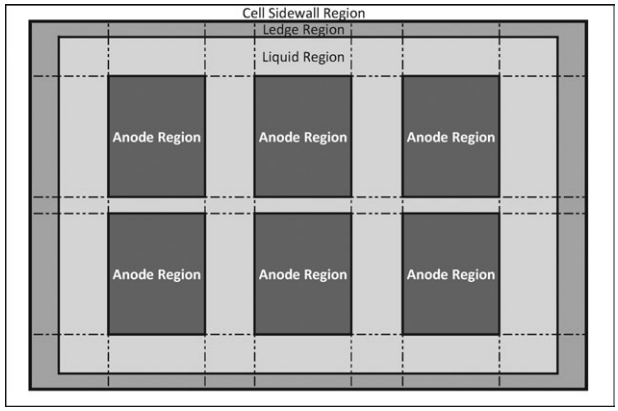

Figure 2. An illustrative discretization of bath and ledge regions.

because the dynamics and the heat exchange mechanism of subsystems can be different due to their own and neighboring environments as imposed by the cell geometry and anode arrangements, even if they are in the same region. The discretization method provides the freedom to construct mass and thermal balance equations as required in different subsystems. Hence, local variations caused by local disturbances can be captured as a function of the location. The availability of individual anode current measurements reveals the overall path resistance across the bath and metal layer. The computation of vertical resistance distribution is not necessary to calculate local ohmic heat generation in the subsystems. Subsystems are, therefore, not further divided into different horizontal layers. In the present approach, each subsystem consists of both the bath layer and the metal layer in the liquid region, with an additional layer of anode block in subsystems where an anode is present.

Model features

2-D heat transfer in a reduction cell through ledge and sidewall is computed in this model based on heat equations. Heat dissipation from the cell through the top and the bottom of the reduction cell is estimated by the corresponding heat loss percentages of a typical reduction cell.[25,40] The model takes individual anode currents and cell voltage signals as major inputs to calculate temperature distribution and boundary shift between ledge and bath region based on the subsystems' structure. Bath and metal heights can be deduced and their sum defines the height of the volume of interest in this approach. Despite the discretization, they are treated as global variables and shared among all the subsystems. This also applies to the computation of liquidus temperature. In this model, the bath composition changes only when the bath volume changes. It is assumed that alumina feeding rate is equal to the consumption rate. Heats of dissolution and reaction are converted to equivalent voltages and excluded from the computation of heat generation. Hence, their impacts on the thermal balance are averaged out. Current efficiency at each anode is assumed to be the same, except shorting anodes. Temperature and mass of bath as well as ledge of subsystems, anode height, and metal production are states in the model. They are all interdependent and solved simultaneously in MATLAB. The following section describes different types of thermal balances and mass balances considered in the model, resulting from various cell environments.

Thermal and Material Balances

Thermal balances of subsystems in the proposed approach are all derived from the general heat equation. In this 2-D heat exchange model, thermal balance equations always consist of several terms to describe the rate of heat transfer present at interfaces, each for one different direction as denoted by q^k. The superscript, k, represents the type of interface for different cases, as detailed in the following sections. On the other hand, the subscripts denote the direction of the heat flow to the subsystem (i,j) from its neighboring subsystems. The thermal balance equation is given as

$$\frac{\mathrm{d}(\bar{C}\cdot T_{i,j})}{\mathrm{d}t} = q^k_{i-1,j} + q^k_{i+1,j} + q^k_{i,j-1} + q^k_{i,j+1} + q_{\mathrm{ohmic}}, \qquad (4)$$

for all $i = 1, \ldots, N_x$, and $j = 1, \ldots, N_y$, where N_x and N_y are the number of subsystems in x and y directions, respectively. The thermal capacity is denoted by $\bar{C}$, whereas the temperature of subsystem (i, j) is represented by $T_{i,j}$. For subsystems where there is no anode present

$$q_{\mathrm{ohmic}} = 0,$$

as heat generation only takes place where the current passes. Balances are characterized by the regions where the subsystems are located, followed by the interface at the boundaries. Therefore, thermal balances can be slightly different from others in the same region corresponding to their subsystem locations. There are 10 different cases considered in this model in three different regions. The following section describes different type of heat transfer rate that are used in the conjunction of Eq. 4. Mass balance of bath and ledge are also discussed. Subscripts of b, m, an, and L, indicate systems of bath, metal, anode, and ledge, respectively. A bar on top of a variable indicates that it represents either a physical or thermal property. Symbols with a tilde (~) are global variables. Otherwise, they are localized variables and can be different in subsystems. Numbering of subsystems in examples below follows Figure 3.

Liquid region

The liquid region consists of two different types of subsystems. As previously described, subsystems in this region take both the bath and metal layers into consideration and sometimes an anode layer when an anode is present. The first type describes the heat transfer of liquids in subsystems without any anodes present. There are five types of interface considered in this approach.

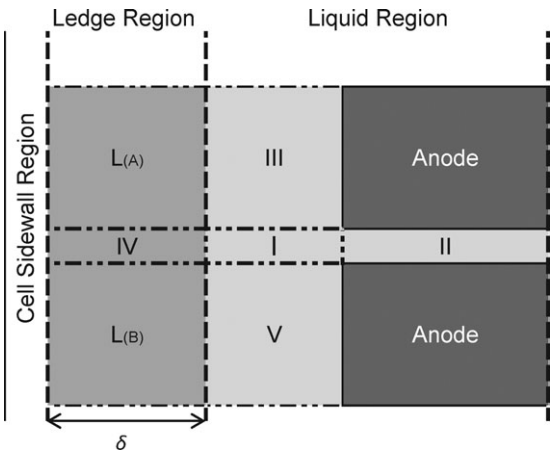

Figure 3. Discretization of the liquid region.

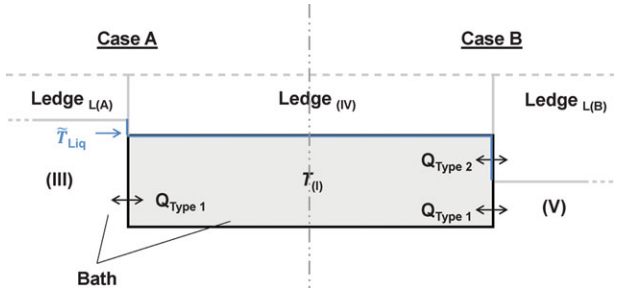

Figure 4. Examples of heat transfer near the ledge.

[Color figure can be viewed in the online issue, which is available at wileyonlinelibrary.com.]

Liquid–Liquid Interface (Cases 1, 2, and 3). When a subsystem, for example, (I), and one of its neighbors, for example, (II), do not consist of an anode as illustrated in Figure 3, only liquid is involved in the heat transfer at the boundary between these two subsystems. As both the bath height $\tilde{H}_{\mathrm{b}}$, and metal height $\tilde{H}_{\mathrm{m}}$, are global variables across the liquid region, bath layer only interfaces with bath layers of neighboring subsystems at the interface they share. The condition where bath and metal layer interfaces at a subsystem boundary does not exist. Therefore, horizontal heat exchange between bath and metal layers is not considered in this approach. The same applies for the metal layer. In this preliminary study of spatial temperature variations, heat convection caused by liquid flow in a reduction cell are captured by implementing higher thermal conductivities of bath $\bar{k}_{\mathrm{b}}$, and metal $\bar{k}_{\mathrm{m}}$, in the computation as proposed elsewhere in the literature.[41]

Bruggeman et al.[42] computed an equivalent conduction term to compensate the thermal effect caused by bulk convection using the Peclet number. The Peclet number defines the ratio of heat transfer of convection to conduction of which is the dominant heat transfer in a system. The impact of conduction on heat transfer is the same as convection when the Peclet number is equal to 1. The resulting thermal conductivity thus takes into account the heat flow by the flowing liquid. The result obtained in their study is 17,000 W m^{-1} K^{-1}. That study also suggests that cell heat loss and ledge formation are insensitive to bath and metal conductivities when they are greater than 400 W m^{-1} K^{-1} and 1600 W m^{-1} K^{-1} respectively, based on numerical computation. Therefore, different choices of enhanced thermal conductivities do not lead to significant deviation from each other in the range stated above. Based on industrial observations, highly enhanced thermal conductivities of bath and metal of 3000 W m^{-1} K^{-1} are used in this study to reduce the thermal gradient within the liquid region.

The rate of heat flow at this type of interface q^1, (i.e., $k = 1$ in Eq. 4) is determined by

$$q^1 = \left(\frac{\bar{k}_{\mathrm{b}}\cdot A_{\mathrm{b}}(\tilde{H}_{\mathrm{b}}) + \bar{k}_{\mathrm{m}}\cdot A_{\mathrm{m}}(\tilde{H}_{\mathrm{m}})}{d}\right)\left(T_{\mathrm{b(II)}} - T_{\mathrm{b(I)}}\right), \qquad (5)$$

with d, as the distance between the center points of the subsystems. This equation describes the heat transfer from subsystem (II) through the right hand interface of subsystem (I). As bath and metal height can change as a function of time, cross sectional area of bath layer A_{b}, and metal layers A_{m}, that are perpendicular to the heat flow change with respect to their corresponding heights. In the case where subsystems, for example, (I), (III), and (V), are located next to the ledge as shown in Figures 3 and 4, the cross-sectional area also changes with the ledge thickness δ. As ledge thickness of subsystems

next to each other can be different due to local superheat, two possible types of heat exchange mechanism exist for this type of subsystems as illustrated in Figure 4. Case A, on the left of the figure, shows the situation where only liquid–liquid conduction Q_{Type1}, occurs. This type of heat transfer takes place when the relative thickness of the ledge adhered to the interested subsystem is greater than that of neighbor's. Therefore, the rate of heat transfer from subsystem (III) to subsystem (I) through their shared boundary can be described by Eq. 5. In the situation illustrated in Case B, conduction at liquid-ledge Q_{Type2}, interface also occurs as a result of the greater relative ledge thickness of L(B). Heat transfer rate from subsystem (V) to subsystem (I) is given by

$$q^2 = \left(\frac{\bar{k}_{\text{b}} \cdot A_{\text{b}}(\tilde{H}_{\text{b}}, \delta_{(\text{IV})}) + \bar{k}_{\text{m}} \cdot A_{\text{m}}(\tilde{H}_{\text{m}}, \delta_{(\text{IV})})}{d}\right) \cdot \left(T_{\text{b(V)}} - T_{\text{b(I)}}\right) - \left(\bar{h}_{\text{b}} \cdot A_{\text{b}}(\tilde{H}_{\text{b}}, \delta_{(\text{IV})}, \delta_{\text{L(B)}}) + \bar{h}_{\text{m}} \cdot A_{\text{m}}(\tilde{H}_{\text{m}}, \delta_{(\text{IV})}, \delta_{\text{L(B)}})\right) \cdot \left(T_{\text{b(I)}} - \tilde{T}_{\text{Liq}}\right). \quad (6)$$

Heat transfer coefficients between bath and ledge $\bar{h}_{\text{b}}$, and between metal and ledge $\bar{h}_{\text{m}}$, range from 830 W m^{-2} K^{-1} to 1600 W m^{-2} K^{-1} and 400 W m^{-2} K^{-1} to 1500 W m^{-2} K^{-1} in literature.[17,26,40,43,44] As the focus of the model is to compute the change of ledge thickness based on the variation of anode current distribution, rather than the absolute thickness, the choice of heat transfer coefficients is not crucial in this article. Therefore, the model implements heat transfer coefficients with $\bar{h}_{\text{b}}$ of 1200 W m^{-2} K^{-1} and $\bar{h}_{\text{m}}$ of 700 W m^{-2} K^{-1} for simulation studies in this work.

As the relative thickness of ledge in the subsystems can change, a conditional term is introduced to account for both possible mechanisms between ledge subsystem. An example of heat transfer between (I) and (V) is expressed as

$$q^3 = \begin{cases} q^1 & \delta_{(\text{IV})} \geq \delta_{\text{L(B)}} \\ q^2 & \delta_{(\text{IV})} < \delta_{\text{L(B)}}. \end{cases} \quad (7)$$

Liquid/Ledge Interface (Case 4). In the case of a subsystem, for example, (I) is located next to a subsystem of ledge, for example (IV), heat transfer takes place between the interface of liquid and ledge. As the interface is assumed to be always at the liquidus temperature, the heat transfer rate between these two subsystems q^4, is given as

$$q^4 = -\left(\bar{h}_{\text{b}} \cdot A_{\text{b}}(\tilde{H}_{\text{b}}) + \bar{h}_{\text{m}} \cdot A_{\text{m}}(\tilde{H}_{\text{m}})\right) \cdot \left(T_{\text{b(I)}} - \tilde{T}_{\text{Liq}}\right). \quad (8)$$

Liquid/Anode Interface (Case 5). This interface arises when a neighboring subsystem consists of an anode. As the bath height changes as a function of time, the depth of an anode immersed in the bath varies accordingly. This variation is captured by including ACD in the computation of cross sectional area of the heat flow to the anode. The heat transfer rate is expressed as

$$q^5 = -\bar{h}_{\text{an}} \cdot A_{\text{an}}(\tilde{H}_{\text{b}}, \text{ACD}) \cdot \left(T_{\text{b(III)}} - T_{\text{b(an)}}\right) + \left(\frac{\bar{k}_{\text{b}} \cdot A_{\text{b}}(\text{ACD}) + \bar{k}_{\text{m}} \cdot A_{\text{m}}(\tilde{H}_{\text{m}})}{d}\right)\left(T_{\text{b(an)}} - T_{\text{b(III)}}\right), \quad (9)$$

where $\bar{h}_{\text{an}}$, is the heat transfer coefficient at the anode surface in contact with bath.

Anode Region. In this work, it is assumed that anode current only travels from the anodes directly to the cathode without spreading to neighboring subsystems. Therefore, only subsystems that consist of an anode are the heat sources in the cell. This approach does not require the computation of heat dissipation caused by each physical component separately. The ohmic voltage drop V_{ohmic}, as described in Eq. 2, defines the voltage drop from the bath surface to the carbon cathode surface as shown in Figure 1. Therefore, the heat generation term q_{ohmic}, includes heat generated from all physical components in the subsystem. When uneven anode current distribution arises in the cell q_{ohmic}, in the thermal balance described in Eq.4 takes into account the local energy input to this type of subsystems, which varies with the flow of anode currents. The calculation of heat flow rate at the interface is the same as q^5 expressed in Eq. 9.

Ledge region

Subsystems in this region are only made up of ledge. Ledge thickness can change through the freezing and melting process, therefore, the subsystems' dimension can change in the direction perpendicular to the adhered sidewall. The degree of change for each subsystem is determined by the local superheat. The local superheat is defined as the difference between the bath temperature of the immediate liquid subsystem and the global liquidus temperature. As the interface between the bath and ledge is at liquidus temperature, freezing and melting only occurs at the surface. The mass balance of the subsystem becomes

$$\frac{\text{d}(m_{\text{L}})}{\text{d}t} = \frac{q^6 + q^4}{\Delta \bar{H}_f}, \quad (10)$$

where m_{L} is the mass of the ledge in the subsystem with $\Delta \bar{H}_f$ being the heat of fusion of cryolite. The heat flow rate q^4, which has been previously discussed, also describes the local thermal driving force to the ledge. On the other hand, q^6 expresses the rate of local heat flows to the ledge subsystem, discussed in the next section. Ledge thickness of subsystems altogether gives the ledge profile. The profile defines the boundary between the solidified bath and the liquid. The change of profile determines the amount of bath removed or released during the freezing and melting process, and the cross-sectional area of the cell cavity. Bath volume as well as the height can be deduced as a function of ledge thickness as follows

$$\bar{\rho}_{\text{b}} \frac{\text{d}(\tilde{H}_{\text{b}} \cdot A(\delta))}{\text{d}t} = -\sum \frac{\text{d}(m_{\text{L}})}{\text{d}t} \quad (11)$$

with $\bar{\rho}_{\text{b}}$, as the density of the liquid bath.

Ledge/Nonledge Interface (Cases 6 and 7). For a ledge subsystem, for example (IV), the rate of heat flow perpendicular from the ledge surface is defined as

$$q^6 = \left(\frac{\bar{k}_{\text{L}}(\tilde{H}_{\text{b}}, \tilde{H}_{\text{m}})}{d}\right) \cdot \left(\tilde{T}_{\text{Liq}} - T_{\text{L(IV)}}\right). \quad (12)$$

Similarly, heat flow rate to the sidewall is determined by

$$q^7 = \left(\frac{1}{R_{\text{sw}} + R_{\text{L}}}\right) \cdot \left(\bar{T}_{\text{sw}} - T_{\text{L(IV)}}\right), \quad (13)$$

where R_{sw} and R_{L} are the thermal resistance of the cell sidewall and the ledge, respectively. Resistance of the sidewall can vary due to the design of different cell technology.

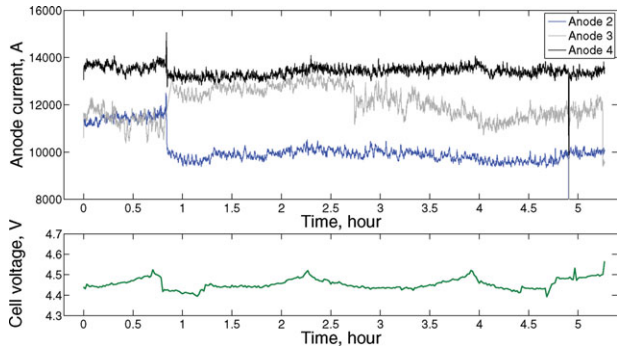

Figure 5. Anode current profiles and cell voltage.

[Color figure can be viewed in the online issue, which is available at wileyonlinelibrary.com.]

Ledge/Ledge Interface (Cases 8, 9, and 10). Temperature variation across the liquid region leads to differences in local superheat. Consequently, the relative ledge thickness can be uneven. Therefore, heat transfer of subsystems in the ledge region is conditional; similar to subsystems in the liquid region when they are located next to the ledge. To account for different heat exchange mechanisms taking place side-by-side to a ledge subsystem, conditional terms need to be included in the heat equation for subsystems of ledge. The heat transfer between (IV) and L(A) is given as

$$q^8 = \begin{cases} q^9 & \delta_{(\mathrm{IV})} \le \delta_{\mathrm{L(A)}} \\ q^{10} & \delta_{(\mathrm{IV})} > \delta_{\mathrm{L(A)}}. \end{cases} \tag{14}$$

The heat transfer rate q^9, describes the heat exchange between ledge subsystems by conduction.

$$q^9 = \left(\frac{\bar{k}_{\mathrm{L}} \cdot A_{\mathrm{L}}(\tilde{H}_{\mathrm{b}}, \tilde{H}_{\mathrm{m}}, \delta_{(\mathrm{IV})})}{d} \right) \left(T_{\mathrm{L(A)}} - T_{\mathrm{L(IV)}} \right). \tag{15}$$

On the other hand, q^{10}, expresses the heat transfer rate occurs due to partial exposure of side ledge to the bath as illustrated in Figure 4.

$$q^{10} = \left(\frac{\bar{k}_{\mathrm{L}} \cdot A_{\mathrm{L}}(\tilde{H}_{\mathrm{b}}, \tilde{H}_{\mathrm{m}}, \delta_{\mathrm{L(A)}})}{d} \right) \cdot \left(T_{\mathrm{L(A)}} - T_{\mathrm{L(IV)}} \right) - \bar{h}_{\mathrm{b-L}} \cdot A_{\mathrm{L}}(\tilde{H}_{\mathrm{b}}, \tilde{H}_{\mathrm{m}}, \delta_{(\mathrm{IV})}, \delta_{\mathrm{L(A)}}) \cdot \left(T_{\mathrm{L(IV)}} - \tilde{T}_{\mathrm{Liq}} \right). \tag{16}$$

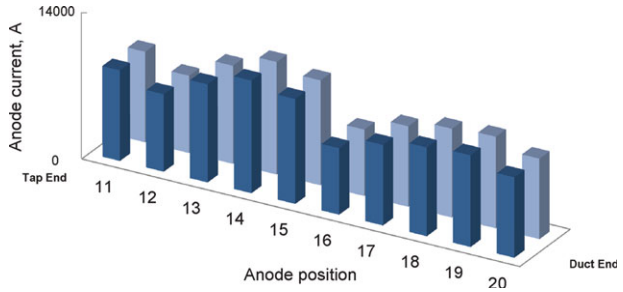

Figure 6. An example of anode current distribution in an operating cell.

[Color figure can be viewed in the online issue, which is available at wileyonlinelibrary.com.]

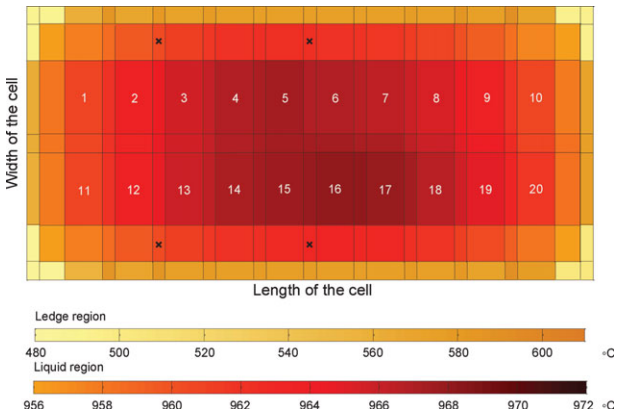

Figure 7. Temperature distribution at initial state.

[Color figure can be viewed in the online issue, which is available at wileyonlinelibrary.com.]

Sidewall region

In this preliminary model, the sidewall region is not discretized as in the liquid region and ledge region. The focus is to investigate the impact of current distribution on the thermal balance. Therefore, the computation of sidewall temperature is based on 1-D heat transfer. In other words, it only gives the temperature in the middle of the sidewall. Surface temperature of the sidewall is also calculated in a similar way.

In the following sections, local thermal condition of a reduction cell consists of 20 anodes was studied. Based on the proposed discretization method, the thermal model has 161 subsystems with a total of 242 interacting states.

Model Validation

Process data were obtained from an operating reduction cell for model validation. This set of data includes approximately 5½ h of continuous anode current and cell voltage signals. Anode 3 was deliberately lowered during the operation at $t = 0.8$ h. It caused abrupt change on the anode currents as shown in the examples of anode current profiles in Figure 5. Respective cell voltage is also included in the

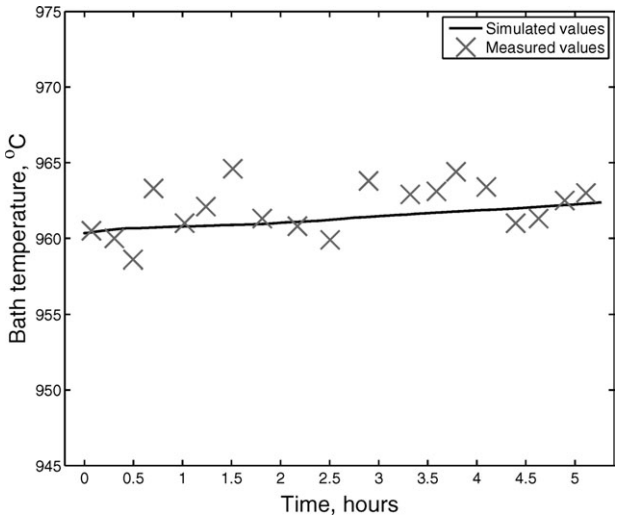

Figure 8. Simulated and measured bath temperatures (located between Anode 2 and 3).

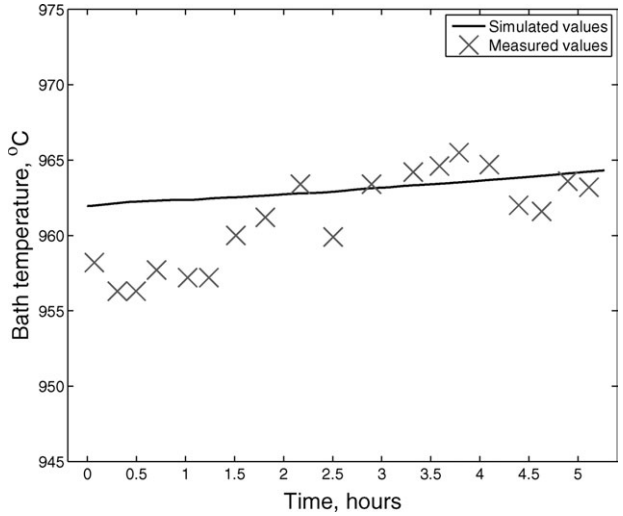

Figure 9. Simulated and measured bath temperatures (located between Anode 5 and 6).

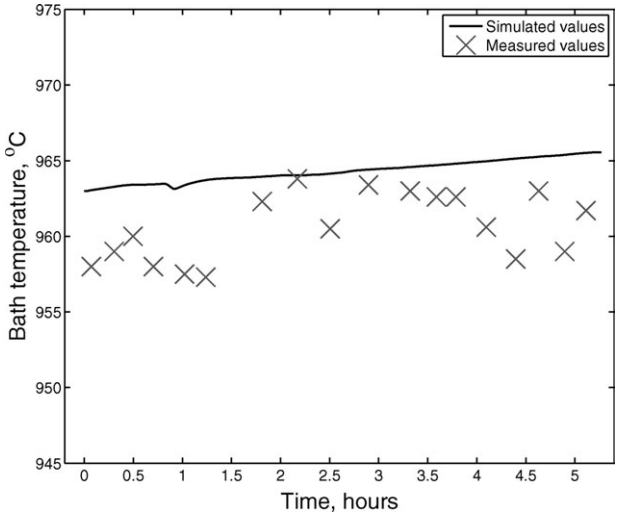

Figure 11. Simulated and measured bath temperatures (located between Anode 15 and 16).

figure. The model has been run with the first set of data obtained from the series of signals as constant inputs to search for an initial condition close to the early state of the cell condition. As the reduction cell studied has an uneven current distribution as shown in Figure 6, the resulting temperature distribution at the initial state is not uniform. This is depicted in Figure 7 marked with anodes number.

Spot bath temperature measurements were conducted at different locations to observe the change of cell condition during this period. Their locations are marked in Figure 7. The series of anode current and voltage signals were input to the model to compute the spatial variations based on the chosen initial condition. The thermal response of subsystems that are close to the measuring locations are compared with the bath temperature measurements and are shown in Figures 8–11.

When comparing simulated and measured temperature values, it should be noted that the measured bath temperature exhibits a combination of slow and fast dynamics. The fast oscillation in temperature is caused by the change in thermal energy associated with alumina feeding. It reflects the reduction of energy each time when alumina is introduced to the bath as energy is extracted for alumina heating and dissolution. An example of bath temperature changes with alumina feeding is illustrated in Figure 12.[3] The significant drop of the measured bath temperature occurs on regular basis usually indicating the start of alumina overfeeding. A small cyclical reduction and subsequent increase in temperature observed in the figure mirror the change in the alumina feeding strategy as part of the cell control. The alumina feed rate generally varies from a feed rate that is in excess of the calculated requirement to one that is lower than theoretically needed.

The simulated temperature trend matches the slow linear increase in bath temperature and not the superimposed fast dynamics. This is because, as previously described, energy in the cell associated with feeding has been excluded from the ohmic heat generation in the present model by subtracting the respective equivalent voltage from the cell voltage. Thus, the fast oscillations associated with alumina feeding are not reflected in the simulation. The simulation result shows the increase of bath temperature as a result of anode current distribution. Thermal response of the cell associating feedings will be considered in future iterations of the model development.

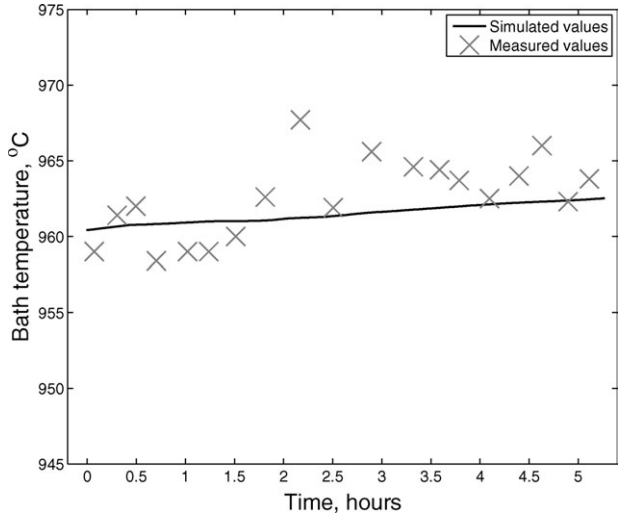

Figure 10. Simulated and measured bath temperatures (located between Anode 12 and 13).

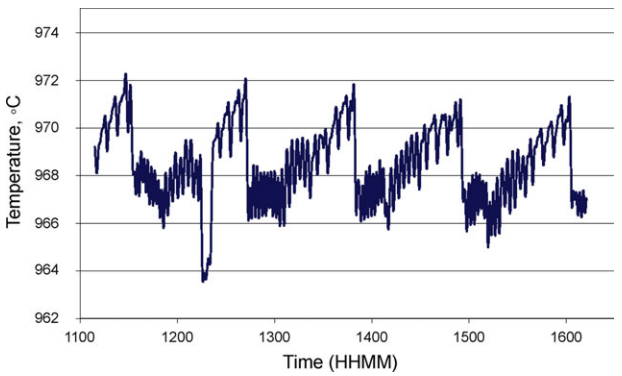

Figure 12. Measured temperature profile, reproduced from Whitfield (2003).[3]

[Color figure can be viewed in the online issue, which is available at wileyonlinelibrary.com.]

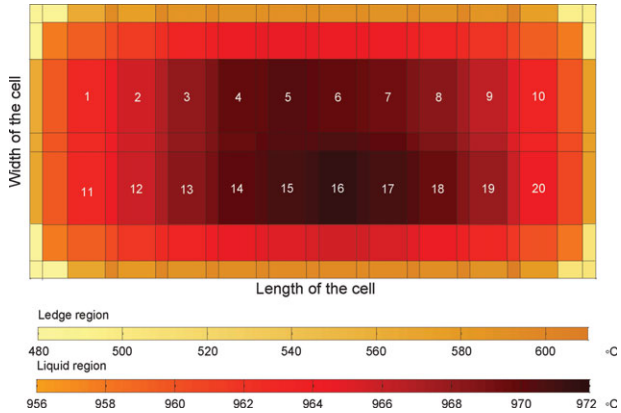

Figure 13. Model validation: simulated temperature distribution at final state.

[Color figure can be viewed in the online issue, which is available at wileyonlinelibrary.com.]

Process data available in this validation study are insufficient to determine the full initial condition of the cell. It is because at least equivalent numbers of measurements to the number of states is required. The best initial condition that can possibly be obtained, therefore, only partly matches the early state of the cell condition. The initial condition between Anode 15 and 16 has the highest deviation from the measured value. As a result, the simulated values are higher than the measured values. However, the overall change matches the total increase of the measured bath temperature. Figure 13 shows the simulated temperature distribution at the final state of the simulation.

Spatial temperature measurements conducted at different locations in this study are shown in Figure 14. Cooler bath temperatures at the centers of the side channel (between Anode 5 and 6, and between Anode 15 and 16) are observed because there are a recent replacement of Anode 7. Its impact to the temperature in the proximity causes a reduction of temperature. As this effect is not captured by this proposed model, the measurements show different spatial temperature distribution to the model computation. The measurements conducted in this study, and other works found in the literature,[3,4] suggest a measured temperature at

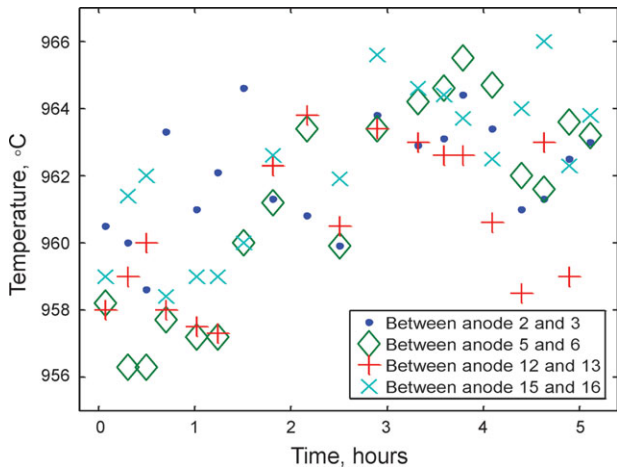

Figure 14. Temperature measurements at different cell locations.

[Color figure can be viewed in the online issue, which is available at wileyonlinelibrary.com.]

Table 1. Summary of Shorting Anodes in Each Simulation Study

Simulation Study	Shorting Anode(s)
Case S0 (reference case)	None
Case S1	Anode 2
Case S2	Anode 5 and 6
Case S3	Anode 2 and 5

a specific location can have an offset of the order of ±3 to ±5°C from the average temperature within the cell. However, this is strongly dependent on the cell design and operating features including anode replacement pattern.

Simulation Studies—Results and Discussion

The validation demonstrates that the model has the ability to predict the overall trend of the cell thermal response as a function of location by importing anode currents and voltage signals. Simulation studies in the following section investigate the impact of uneven current distribution induced by anode shorting on the local thermal conditions. Spatial variations of temperature and ledge thickness can be deduced based on anode current signals. They are usually not considered in conventional thermal models.

Anode shorting

Anodes in the bath are held by anode beams and suspended above the metal layer with a specific ACD. Uniform ACD of all anodes within a cell is required for even current distribution to be achieved. During setting, new anodes are generally positioned higher than the other anodes such that the anode surface will end up at the same level as the others after it reaches full carrying current capacity. Anode slip sometimes occurs in an operating cell if an anode rod is not held by the clamp properly. The anode would slowly slip through the clamp and fall deeper into the bath. As a carbon anode has a higher electrical conductivity than the electrolyte, more current would flow into the shorting anode, enter the metal layer without producing any metal. This is one of the process abnormalities that sometimes occurs at an individual anode, causing a localized thermal imbalance. It is hard to identify by conventional measurements until the effect propagates through the entire cell and affects the productivity.[25,33]

Simulation studies of shorting anodes were carried out to investigate the impact on cell temperature and ledge thickness as a function of time and location. The worst case of anode shorting is assumed in the simulation studies where the anode surface completely touches the metal layer at the cathode. In such case, no electrochemical reactions take

Table 2. Initial Condition for Simulation Studies

Cell Technology	
Cell width and length	4 × 9.5 m^2
Anode	20
Cell Parameters	
Bath height	16 cm
Metal height	21 cm
Anode height	59 cm
Sidewall temperature	334°C
Shell surface temperature	312°C
Liquidus temperature	951.8°C

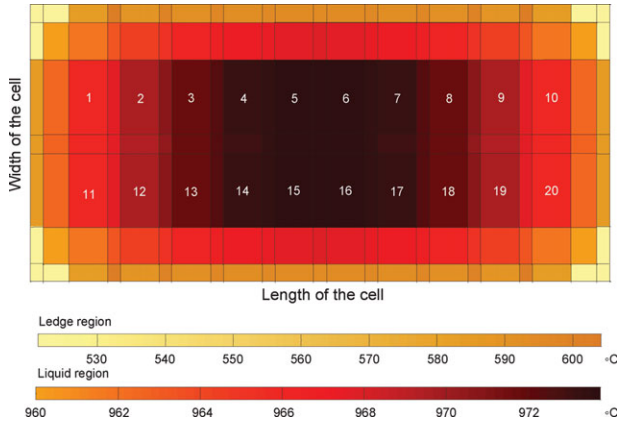

Figure 15. Temperature profile across the bath and legion region at initial state (t = 0 h).

[Color figure can be viewed in the online issue, which is available at wileyonlinelibrary.com.]

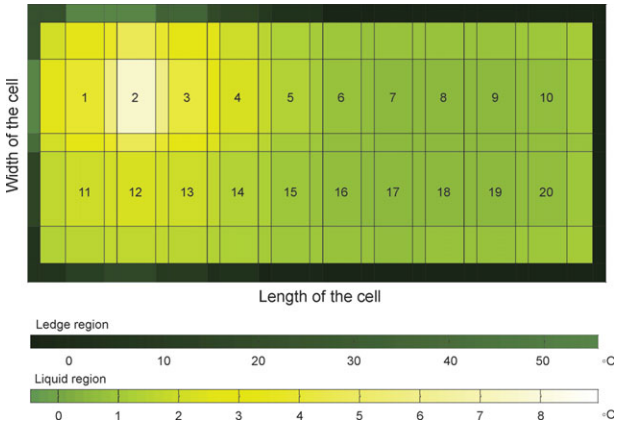

Figure 17. Temperature deviation T', across the cell at t = 5 h (Case S1).

[Color figure can be viewed in the online issue, which is available at wileyonlinelibrary.com.]

place at the fully shorting anode. Therefore, the current efficiency at this particular anode reduces to zero. Energy that contributes to the electrochemical reactions during normal operation dissipates as heat in the cell. As a result, the increase of ohmic voltage enhances the local heat generation. For the purpose of the simulation, a shorting anode is defined as occurring when the anode current exceeds 1.5 times the average. In the following simulation studies, a shorting anode is set to carry 1.5 times the average line current at $t = 0$ h while the remaining current is equally distributed among all other normal anodes. Table 1 summarizes the cases studied. Locations of anodes are marked in heat maps presented in the later sections. A simulation without any shorting anode, Case S0, was also conducted to define the baseline for other cases. As the system never reaches steady state due to the continuous anode consumption, it provides a better reference for comparison. In an operating cell, cell voltage is always closely monitored and kept within the controller band. It is, therefore, assumed that the cell voltage does not vary during the simulation.

Initial condition

All simulation studies presented in this article were conducted based on the same initial condition. The chosen initial condition exhibits a similar cell condition to operating smelters. Parameters are listed in Table 2 and shown in Figure 15. Bath temperature across the bath is the highest at the center and lowest near the sidewall. This is because subsystems close to the sidewall have greater heat loss and are further from the heat sources. As bath flow is not considered in this model, temperature differences within the cell are expected to be greater than in an operating cell. As constant uniform current distribution is applied to the model to obtain the initial condition, temperature across the cell and ledge profile of the initial condition is symmetric. In addition, anodes are set to be at the same height because they are assumed to be at the same service life. Therefore, the symmetric temperature profile at initial state is different from the case of model validation.

Case S1

Energy redistribution within a cell caused by a shorting anode is reflected by the temperature deviated, T' from the reference case, Case S0. Figures 16–18 show the change in temperature as a function of time. The shorting anode causes a significant localized increase in temperature at the surrounding at $t = 1$ h due to the enhanced ohmic voltage. As the amperage of the cell is regulated and kept constant,

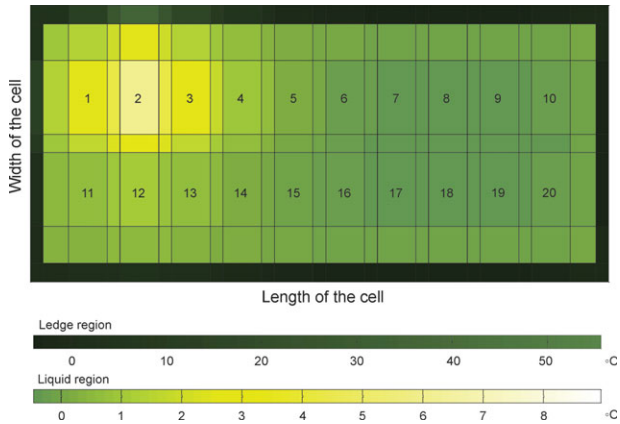

Figure 16. Temperature deviation T', across the cell at t = 1 h (Case S1).

[Color figure can be viewed in the online issue, which is available at wileyonlinelibrary.com.]

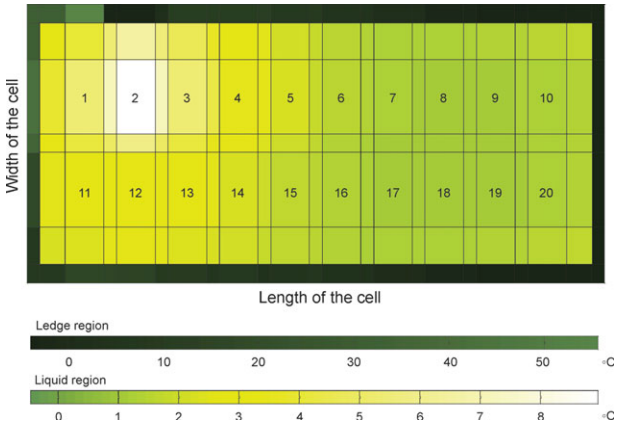

Figure 18. Temperature deviation T', across the cell at t = 8 h (Case S1).

[Color figure can be viewed in the online issue, which is available at wileyonlinelibrary.com.]

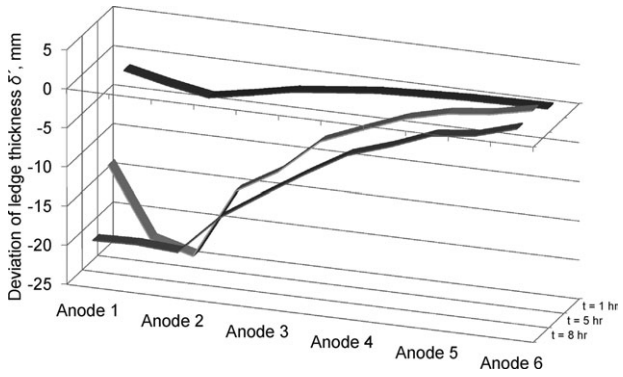

Figure 19. Deviation of ledge thickness δ' at upstream near tap end (Case S1).

energy input to the rest of the anodes has been reduced. This causes the temperature in those regions to decrease slightly. The thermal effect caused by shorting then propagates across the cell, leading to an increase of an average of 1.5°C on the overall bath temperature at $t = 8$ h. Although the total energy input is the same, the effect does not even out because the rate of heat dissipation through the ledge and sidewall does not balance the heat increases in the bath. Heat accumulates in the cell and, thus, bath temperature increases. Some of the heat transferred to the ledge as reflected by the change in temperature distribution. Temperature of the ledge subsystem close to Anode 2 increases at the beginning, then decreases during the course of the simulation. This is because the energy is absorbed by the ledge through the melting process. The change in ledge profile with respect to Case S0 at different times in the simulation is illustrated in Figure 19. Ledge thickness near Anode 2 decreases significantly as the shorting continues. There is a slight increase of ledge thickness at $t = 8$ h because the local superheat changes as the ledge melting causes a variation of liquidus temperature. As the overall bath temperature has increased, local superheat causes the ledge thickness decreases to different extents. There is a total of 17.8 kg of ledge melted when the simulation reaches $t = 8$ h. It corresponds to approximately 9000 kJ of energy absorbed by the ledge. This melted ledge takes away the heat and slightly changes the heat loss from the bath through the sidewall.

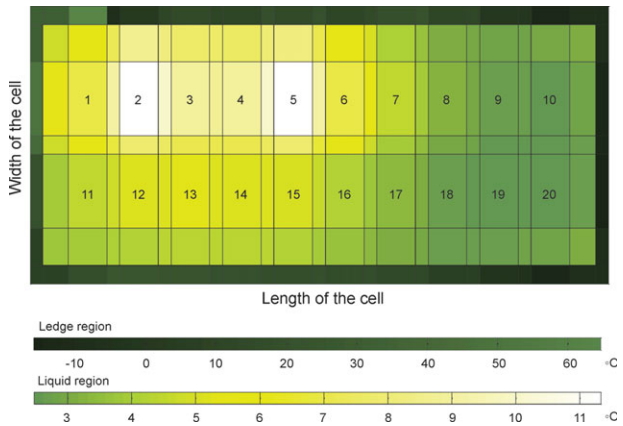

Figure 20. Temperature deviation T', across the cell at $t = 8$ h (Case S2).

[Color figure can be viewed in the online issue, which is available at wileyonlinelibrary.com.]

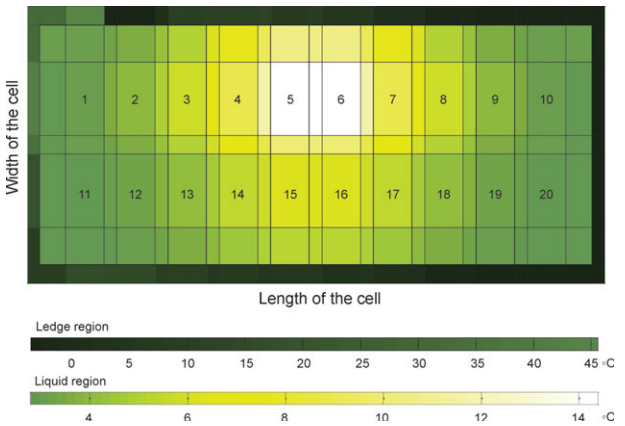

Figure 21. Temperature deviation T', across the cell at $t = 8$ h (Case S3).

[Color figure can be viewed in the online issue, which is available at wileyonlinelibrary.com.]

The accuracy of the simulated results depends on the chosen initial condition to the actual industrial condition, whether the same in current efficiency is being maintained, and of course the accuracy of the thermodynamic database used. As this model does not consider heat convection caused by the bath flow, the energy transfer may respond faster than the model predicts.

Cases S2 and S3

These case studies investigate the change in spatial temperature distribution caused by multiple anode shortings. Different pairs of anodes are selected to study the impacts on cell thermal balance as a function of relative distance between shorting anodes. Deviation in temperature distribution for both cases at $t = 8$ h are shown in Figures 20 and 21. Shorting anodes in Case S2 are two anodes apart from each other, extra current is diverted to those anodes leading to a localized increase in energy as depicted in the temperature distribution. The localized increase in energy is not as concentrated and significant as in Case S3 as shorting anodes are located next to each other. As previously discussed, energy in the bath cannot dissipate fast enough through the sidewall. As two anodes experience shorting in both cases, the overall increase of temperature is greater compared to Case S1. The energy redistribution in the bath leads to a localized meltdown of ledge at the vicinity of the shorting anodes. Ledge profiles close to the shorting anodes for both cases are shown in Figures 22 and 23

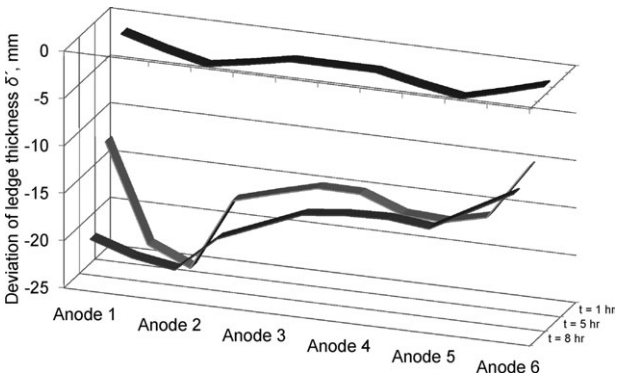

Figure 22. Deviation of ledge thickness δ', at upstream near tap end (Case S2).

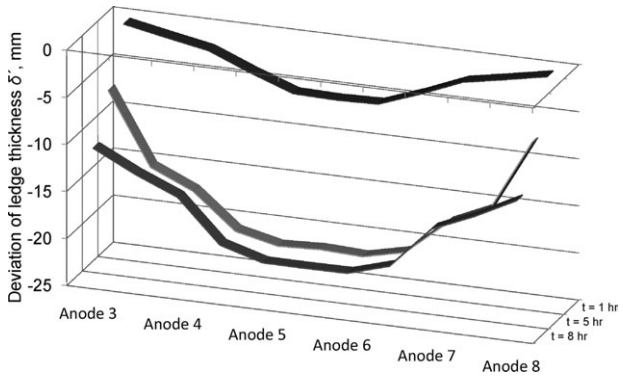

Figure 23. Deviation of ledge thickness δ', at upstream at the center of the cell (Case S3).

as a function of time. Assuming constant current efficiency, the model predictions indicate that 8 h of shorting would cause an overall ledge reduction by approximately 75 kg and 60 kg in Cases S2 and S3, respectively. That means approximately 39,000 and 32,000 kJ of energy have been converted to melting the ledge in each of the respective cases. These values may vary in industrial cells with different designs and initial conditions. The resulting difference of the simulated values is caused by the relative distance of shorting anodes. Temperature increase is more distributed across the bath when shorting anodes are far apart from each other. Larger ledge region is affected. Therefore, greater amount of ledge is melted in Case S2. The simulation studies show the impact of the cell thermal balance and the ledge profile caused by uneven current distribution as a function of time and location. In cases when the current distribution is more uneven, its influences on the thermal balance is more significant as demonstrated in Cases S2 and S3.

Conclusion and Future Development

Bath temperature measurements shown in the model validation section demonstrate that the overall thermal dynamics of the Hall–Héroult process are the combination of a long-term trend superimposed with temporary, localized variations due to alumina dissolution, consistent with earlier studies.[3] As investigated in the simulation studies, current distribution determines energy distribution in a reduction cell, thus leading to variation in local thermal condition. Both studies demonstrate that temperature distribution can be quite uneven in normal operation depending on routine practices and cell technology. Spatial variation can become significant when a large thermal disturbance is introduced, for instance, due to anode replacement and anode shorting. As a result, a measurement conducted at any location in a reduction cell is usually not a representative temperature. Therefore, the proposed thermal model is useful in studying spatial variation that is less easily observed by measurements. This article presents the idea of capturing thermal response at a localized level by incorporating the anode current distribution as model inputs. A discretization method that allows the computation of local ohmic heat generation is also proposed. The proposed model offers freedom of constructing specific type of equations with respect to locations and heat exchange interfaces. Its implementation and the use of anode current signals in this approach allow calculation of heat generation in different part of the cell as a function of respective local energy input. The model validation and the simulation studies show that the model can be used for two different applications: estimating the change of spatial temperature in the cell by implementing real time anode current and voltage signals, and simulating the impacts of current distribution in different scenarios by altering the anode current inputs to the model. Future development of the model will extend from the current model by including heat associated with bath velocity profile and alumina feeding patterns at different locations. Based on the proposed model, local thermal disturbances caused by the feeding can be included in the equation at subsystems where feeders are located. Bath flow profile can be mapped at each interface to compute the convection induced by the bath velocity. These two features are important as they can affect spatial energy distribution and the rate of heat transfer.

Acknowledgments

This project is financially supported by the CSIRO Cluster on Breakthrough Technologies for Aluminium Production, in collaboration with Dubai Aluminium Company Ltd. In particular, authors acknowledge the kind support and assistance with the experiment from Dr. Maryam Mohamed Al-Jallaf, Dr. Daniel Whitfield, Dr. Adam Sherrif, and Mr. Ali Jassim.

Literature Cited

1. Grjotheim K, Kvande H. *Introduction to Aluminium Electrolysis: Understanding the Hall-Héroult Process*, 2nd ed. Dusseldorf: Aluminium-Verlag, 1993.
2. Thonstad J, Fellner P, Haarberg GM, Hives J, Kvande H, Sterten A. *Aluminium Electrolysis: Fundamentals of the Hall-Héroult Process*, 3rd ed. Dusseldorf: Aluminium-Verlag, 2003.
3. Whitfield DS. Aspects of temperature in aluminium smelting cells, PhD Thesis, School of Chemical Engineering, University of New South Wales, 2003.
4. Kristensen W, Hoskuldsson G, Jonsson O. *Moving towards a zero anode effect frequency while achieving world class key performance indicators*. In: *3rd International Conference on Anode Rodding*, Reykjavik, Iceland, 2005:16–22.
5. Djukanovic G. Aluminum: World market prospects for troubled times. *JOM-J Min Met Mat S* 2009;61:63–66.
6. Taylor MP, Chen JJJ. Advances in process control for aluminium smelters. *Mater Manuf Process*. 2007;22:947–957.
7. Kvande H, Haupin W. Cell voltage in aluminum electrolysis: a practical approach. *JOM-J Min Met Mat S*. 2000;52:31–37.
8. Welch BJ. *Advancing the Hall Héroult electrolytic process*. In: *Proceedings of TMS Light Metals*, Nashville, TN, 2000:17–26.
9. Keniry JT, Barber GC, Taylor MP, Welch BJ. *Digital processing of anode current signals: an opportunity for improved cell diagnois and control*. In: *Proceedings of TMS Light Metals*, New Orleans, LA, 2001:1225–1232.
10. Saksvikroenning T. *Estimation of states in aluminium reduction cells applying extended Kalman filtering algorithm together with a nonlinear dynamic model and discrete measurements*. In: *Proceedings of TMS Light Metals*, Las Vegas, NV 1976:275–286.
11. Sorheim EA, Borg P. *Dynamic model and estimator for online supervision of the alumina reduction cell*. In: *Proceedings of TMS Light Metals*, Las Vegas, NV, 1989:379–384.
12. Tikasz L, Bui RT, Potocnik V. Aluminium electrolytic cells: a computer simulator for training and supervision. *Eng Comput*. 1994;10:12–21.
13. Yurkov V, Mann V. *A simple dynamic realtime model for aluminum reduction cell control system*. In: *Proceedings of TMS Light Metals*, San Francisco, CA, 2005:423–428.
14. Piskazhova TV, Mann VC. The use of a dynamic aluminum cell model. *JOM-J Min Met Mat S*. 2006;58:48–52.
15. Kolas S, Støre T. Bath temperature and AlF_3 control of an aluminium electrolysis cell. *Control Eng Pract*. 2009;17:1035–1043.
16. Gusberti V, Severo DS, Welch BJ, Skyllas-Kazacos M. *Modelling the aluminum smelting cell mass and energy balance—a tool based on the 1st law of thermodynamics*. In: *Proceedings of 10th Australian Aluminium Smelting Technology Conference*, Launceston, TAS, 2011.
17. Taylor M, Zhang W, Wills V, Schmid S. A dynamic model for the energy balance of an electrolysis cell. *Chem Eng Res Des*. 1996;74:913–933.

18. Hestetun K, Hovd M. Detection of abnormal alumina feed rate in aluminium electrolysis cells using state and parameter estimation. *Comput Aided Chem Eng*. 2006;21B:1557–1562.
19. Cheung C, Menictas C, Bao J, Skyllas-Kazacos M, Welch BJ. *Dynamic modelling of an operating aluminium reduction cell*. In: *Proceedings of CHEMECA 2011, Sydney*, NSW, 2011.
20. Cheung C, Menictas C, Bao J, Skyllas-Kazacos M, Welch BJ. *Simulation of local cell conditions in a Hall-Héroult process based on individual anode currents*. In: *Proceedings of 10th Australasian Aluminium Smelting Technology Conference*, Launceston, TAS, 2011.
21. Cheung C, Menictas C, Bao J, Skyllas-Kazacos M, Welch BJ. *Impact of anode set on the energy redistribution of PB aluminium smelting cells*. In: *Proceeding of TMS Light Metals*, Orlando, FL, 2012.
22. Habashi F. Hall, Héroult and the production of aluminum. *CIM Bull*. 2002;95:109–113.
23. Brooks G, Cooksey M, Wellwood G, Goodes C. Challenges in light metals production. *Trans Inst Min Metall Sect C*. 2007;9:25–33.
24. Choate WT, Aziz A, Friedman R. *New technology will sustain the U.S. primary aluminium industry*. In: *Proceedings of TMS Light Metals*, San Francisco, CA, 2005:495–500.
25. Grjotheim K, Welch BJ. *Aluminium smelter technology—a pure and applied approach*. Dusseldorf: Aluminium-Verlag Gmbh, 1988.
26. Taylor MP, Welch BJ. Melt/freeze heat transfer measurements in cryolite-based electrolytes. *Metall Mater Trans B*. 1987;18:391–398.
27. Kan H, Wang Z, Shi Z, Ban Y, Cao X, Yang S, Qiu Z. *Liquidus temperature, density and electrical conductivity of low temperature electrolyte for aluminum electrolysis*. In: *Proceedings of TMS Light Metals*, Orlando, FL, 2007:531–535.
28. Berezin A, Piskazhova T, Gritsko V, Tarakanov A, Volokhov I, Polyakov P. *Bath superheat to control electrolysis process*. In: *Proceedings of TMS Light Metals*, Orlando, FL, 2007:545–550.
29. Barnett WM. Measuring current distribution in an alumina reduction cell. U.S. Patent US 4786379, 1988.
30. Schneider MH, Evans JW, Ziegler D, Wright P, Steingart D. *Experiments on wireless instrumentation in Hall cells*. In: *Proceedings of TMS Light Metals*, San Francisco, CA, 2005:407–412.
31. Steingart D, Evans J, Wright P, Ziegler D. *Experiments on wireless measurement of anode current in Hall cells*. In: *Proceedings of TMS Light Metals*, New Orleans, LA, 2008:333–338.
32. Urata N, Evans JW. *The determination of pot current distribution by measuring magnetic fields*. In: *Proceedings of TMS Light Metals*, Seattle, WA, 2010:473–478.
33. Bearne G. The development of aluminum reduction cell process control. *JOM-J Min Met Mat S*. 1999;51:16–22.
34. Barber GC. The impact of anode-related process dynamics on cell behaviour during aluminium electrolysis. PhD Thesis, Department of Chemical and Materials Engineering, The University of Auckland, 1992.
35. Keniry J, Shaidulin E. *Anode signal analysis—the next generation in reduction cell control*. In: *Proceedings of TMS Light Metals*, New Orleans, LA, 2008:287–292.
36. Hvidsten RM, Rye K. *Practical applications of the continuous measurement of individual anode currents in Hall-Héroult cells*. In: *Proceedings of TMS Light Metals*, New Orleans, LA, 2008:329–331.
37. Evans JW, Urata N. *Technical and operational benefits of individual anode current monitor*. In: *Proceeding of 10th Australian Aluminium Smelting Technology Conference*, Launceston, TAS, 2011.
38. Haupin W, Seger EJ. *Aiming for zero anode effects*. In: *Proceedings of TMS Light Metals*, New Orleans, LA, 2001:329–335.
39. Majid NAA, Taylor MP, John JJC, Young BR. Multivariate statistical monitoring of the aluminium smelting process. *Comput Chem Eng*. 2011;35:2457–2468.
40. Biedler P. Modeling of an aluminum reduction cell for the development of a state estimator. PhD Thesis, Department of Mechanical and Aerospace Engineering, West Virginia University, 2003.
41. Consiglieri L, MuñIz MC. Existence of solution for a free boundary problem in the thermoelectrical modelling of an aluminium electrolytic cell. *Eur J Appl Math*. 2003;14:201–216.
42. Bruggeman JN, Danka DJ. *Two-dimensional thermal modeling of the Hall-Héroult cell*. In: *Proceedings of TMS Light Metals*, Anaheim, CA, 1990:203–209.
43. Jessen SW. Mathematical modeling of a hall-héroult aluminum reduction cell. MSc Thesis, School of Electrical Engineering, the Technical University of Denmark, 2008.
44. Severo DS, Gusberti V. *A modelling apporach to estimate bath and metal heat transfer coefficients*. In: *Proceedings of TMS Light Metals*, San Francisco, CA, 2009:557–562.

Manuscript received Jun. 14, 2012, and revision received Sept. 21, 2012.